Probing electronic dead layers in homoepitaxial *n*-$SrTiO_3$(001) films

Cite as: APL Mater. 10, 070903 (2022); doi: 10.1063/5.0098500
Submitted: 9 May 2022 • Accepted: 27 June 2022 •
Published Online: 19 July 2022

S. A. Chambers,[1,a] D. Lee,[2] Z. Yang,[2,3] Y. Huang,[3] W. Samarakoon,[1,4] H. Zhou,[5] P. V. Sushko,[1] T. K. Truttmann,[2] L. W. Wangoh,[1,6] T.-L. Lee,[7] J. Gabel,[7] and B. Jalan[2,a]

AFFILIATIONS

[1] Physical and Computational Sciences Directorate, Pacific Northwest National Laboratory, Richland, Washington 99354, USA
[2] Department of Chemical Engineering and Materials Science, University of Minnesota, Minneapolis, Minnesota 99545, USA
[3] School of Physics and Astronomy, University of Minnesota, Minneapolis, Minnesota 99545, USA
[4] School of Chemical, Biological and Environmental Engineering, Oregon State University, Corvallis, Oregon 97331, USA
[5] Advanced Photon Source, Argonne National Laboratory, Lemont, Illinois 60439, USA
[6] International Business Machines Research–Albany Nanotech Complex, Albany, New York 12203, USA
[7] Diamond Light Source, Ltd., Harwell Science and Innovation Campus, Didcot OX11 0DE, United Kingdom

Note: This paper is part of the Special Topic on Materials Challenges and Synthesis Science of Emerging Quantum Materials.
[a] **Authors to whom correspondence should be addressed:** sa.chambers@pnnl.gov and bjalan@umn.edu

ABSTRACT

We combine state-of-the-art oxide epitaxial growth by hybrid molecular beam epitaxy with transport, x-ray photoemission, and surface diffraction, along with classical and first-principles quantum mechanical modeling to investigate the nuances of insulating layer formation in otherwise high-mobility homoepitaxial *n*-$SrTiO_3$(001) films. Our analysis points to charge immobilization at the buried *n*-$SrTiO_3$/undoped $SrTiO_3$(001) interface as well as within the surface contamination layer resulting from air exposure as the drivers of electronic dead-layer formation. As Fermi level equilibration occurs at the surface and the buried interface, charge trapping reduces the sheet carrier density (n_{2D}) and renders the *n*-STO film insulating if n_{2D} falls below the critical value for the metal-to-insulator transition.

INTRODUCTION

The technological utilization of advanced materials typically involves the formation of interfaces with terrestrial environments. These environments include earth's atmosphere, bodies of natural water, such as streams, lakes, and oceans, and electrochemical cells, among others. In all cases, chemisorption and/or chemical reactions that occur at exposed surfaces can alter the properties of the material, sometimes in substantial ways. At the same time, gaining fundamental understanding of the base-line properties of materials can require preventing contact with such environments or cleaning the surface after such contact to keep the material in a pristine state. Accordingly, both kinds of measurements are of considerable value.

Here, we illustrate the interplay of experiments using samples with natural surface contamination due to atmospheric exposure and clean surfaces as we seek to understand electronic dead-layer formation in a prototypical complex oxide semiconductor, $SrTiO_3$. This phenomenon is typically ascribed to surface depletion in which the near-surface region of a semiconductor is devoid of carriers and, thus, not conductive, despite the presence of ionized dopants throughout the region. For example, in well-studied III–V semiconductors, such as *n*-GaAs(001), dangling bonds on clean surfaces, as well as surface impurities resulting from air exposure, can act as mid-gap acceptors that draw electrons from the sub-surface region as the surface and bulk Fermi levels equilibrate, leaving behind ionized donors but no mobile charge. The result is electronic dead-layer formation that is detected by electronic transport measurements.[1] At the same time, Fermi level pinning at or near mid-gap is typically evident in photoemission measurements for all but certain crystallographic orientations, freshly cleaved and in ultrahigh vacuum.[2–4] Charge trapping at the buried interface was

also inferred by *CV* measurements for *n*-type GaAs(001) epitaxial films grown on undoped substrates and interface states were thought to be responsible.[1] However, the surface is often the point of focus because of the plethora of entities that can accumulate with sufficiently high concentration to act as deep-level acceptors that pin the Fermi level.

Homoepitaxial films of $La_xSr_{1-x}TiO_3$ on undoped $SrTiO_3$(001) (STO) substrates have also been reported to exhibit surface depletion.[5,6] For example, it was suggested in Ref. 5 that, for x = 0.05, dead-layer formation occurs when the near-surface region is depleted of electrons as they flow into unoccupied acceptor surface states, resulting in upward band bending of magnitude ~0.7 eV in air-exposed films. This interpretation is commonly invoked in interpreting transport data for *n*-STO epitaxial films up to the present.[7] However, other studies reveal that bulk single crystals of *n*-STO(001) exhibit no such large upward band bending, at least in the (001) orientation.[8–11] Adsorption of O_2 at 80 K on clean *n*-STO(001) results only in slight (~0.2 eV) upward band bending due to electrons being drawn to and localized at surface-bound O_2 molecules.[12] Moreover, there is no evidence that intrinsic acceptor surface states pin the Fermi level deep in the gap of clean STO(001).[13–15] Understanding and ultimately mitigating dead-layer formation is very important for taking full advantage of complex oxide heterostructures in devices, and combining measurements of samples with and without clean surfaces is a useful way to probe these phenomena. Here, we seek to understand the cause(s) of dead-layer formation in *n*-STO using compositionally and structurally well-defined homoepitaxial films prepared by hybrid molecular beam epitaxy (h-MBE)[16] and investigated in pristine ultra-high vacuum conditions as well as in laboratory air. Our results point to both the *n*-STO surface and the buried *n*-STO/undoped STO interface as contributing to dead-layer formation in *n*-STO.

RESULTS AND DISCUSSION

Electronic transport and x-ray photoelectron spectroscopy (XPS)

Hall and resistivity data taken in laboratory air for a set of stoichiometric, structurally well-ordered $Dy_xSr_{1-x}TiO_3$ films (see the supplementary material for experimental and modeling information as well as supporting data) with the same dopant concentration (x = ~0.01) but different thicknesses (*t*) are clearly suggestive of carrier depletion. We show in Fig. 1(a) sheet carrier concentrations (n_{2D}) extracted from data collected at 300 K as a function of *t*. The n_{2D} value for the 32 nm film is zero because the resistance of this film is too large to measure with the van der Pauw geometry. A linear fit of the n_{2D} values for *t* = 65, 89, and 146 nm crosses the film thickness axis at 41.7 nm, the apparent dead-layer thickness for this $Dy_{0.001}$ $Sr_{0.999}TiO_3$ film set. The slope of the n_{2D} vs *t* line yields the bulk carrier concentration, 2.08×10^{19} cm^{-3}. The trapped charge density within a 42 nm thick dead layer at this volume dopant concentration would be 8.8×10^{13} cm^{-2}. The room-temperature mobilities range from 6.7 to 8.9 cm^2/V s, typical of epitaxial *n*-STO(001).[5,6,16]

To predict the extent of band bending that would be expected if surface depletion is the sole cause of these dead layers, we integrate the one-dimensional Poisson equation using boundary conditions appropriate for a free surface with acceptor states, along with 3D carrier density and dead-layer thickness values from the transport data, and dielectric permittivity of $\kappa = 300$ (a typical room-temperature value for STO bulk crystals and high-quality epitaxial films). This calculation yields a surface potential (ϕ) of 1.1 V dropped across a depletion zone width of 42 nm. Taking the bulk Fermi level to be degenerate with the conduction band minimum (CBM) below the depletion zone, the bands would bend upward toward the surface, placing the valence band minimum (VBM) ~2.1 eV below the Fermi level at the surface, as shown in Fig. 1(b).

We now compare this prediction to the surface potential determined directly by x-ray photoelectron spectroscopy (XPS) based on core-level binding energies that are referenced to the top of the valence band in bulk *n*-STO. The measured Sr $3d_{5/2}$ and Ti $2p_{3/2}$ binding energies (Fig. 2) excited with AlKα x-rays for the $Dy_{0.001}$ $Sr_{0.999}TiO_3$ films with surface contamination present range from 133.71(2) to 133.76(2) eV and from 459.15(2) to 459.18(2) eV, respectively, for the three thicker films. From these binding energies, we conclude that the bands are flat at the surfaces of all films within experimental sensitivity and error, as can be seen by comparing the peak energies with the positions of the green vertical lines labeled flat band (see Fig S2 and accompanying text). Not only do the binding energies fall within <0.1 eV of those expected if the bands are flat and the Fermi level is at the conduction band minimum, but there is no peak broadening relative to spectra for clean, flat-band, bulk $SrNb_{0.01}Ti_{0.99}O_3$(001). Such broadening would reveal the presence of built-in potentials across the probe depth.[17] If surface depletion as modeled in Fig. 1(b) is occurring, the Ti $2p_{3/2}$ and

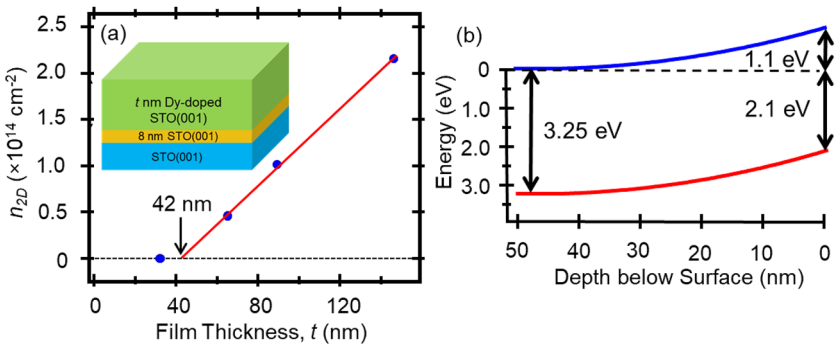

FIG. 1. (a) Measured sheet carrier concentration as a function of film thickness for $Dy_{0.001}$ $Sr_{0.999}TiO_3$ films deposited on $SrTiO_3$(001) with an 8 nm buffer layer of STO. A linear fit to the experimental data indicates a dead-layer thickness of 41.7 nm. (b) Band-edge profile expected if electron transfer to surface states in the gap occurs for a bulk carrier density of 2.08×10^{19} cm^{-3} and a depletion width of 41.7 nm, assuming $\kappa = 300$, based on Poisson modeling.

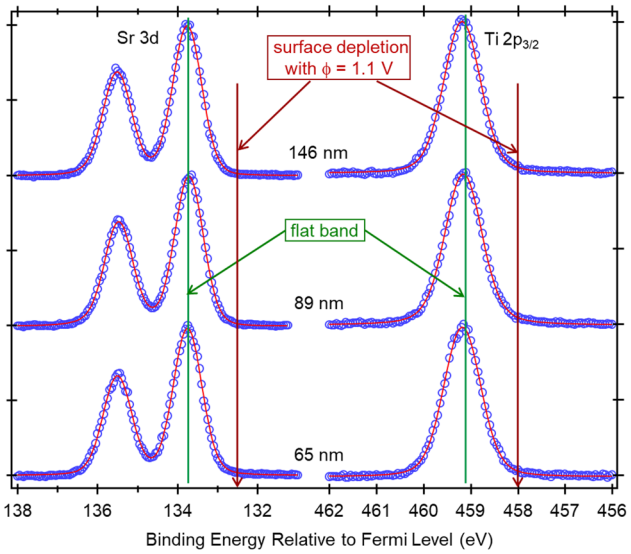

FIG. 2. Sr 3d and Ti $2p_{3/2}$ core-level XPS for t nm $Dy_{0.001}Sr_{0.999}TiO_3$/8 nm $SrTiO_3$/$SrTiO_3$(001) without surface cleaning after the transport measurements in Fig. 1(a) were made. The green and red vertical lines indicate the expected Sr $3d_{5/2}$ and Ti $2p_{3/2}$ binding energies for the flat-band condition and upward band bending of magnitude 1.1 V, respectively.

Sr $3d_{5/2}$ peaks would fall at 132.6(1) and 458.0(1) eV, respectively, which are marked with brown vertical lines in Fig. 2. The energies of the vertical lines are based on the measured photoelectron attenuation lengths for the Sr $3d_{5/2}$ and Ti $2p_{3/2}$ core levels excited with AlKα x-rays in STO (1.91 and 1.45 nm, respectively)[18] being much less than the predicted depletion width (42 nm). In this case, the XPS core-level (CL) measurements would probe only the top few percent of the depletion zone and, thus, directly reflect the full extent of the band bending.

In contrast to the 65, 89, and 146 nm films, the 32 nm film was plagued by surface charging during XPS, revealing insufficient conductivity to facilitate compensation of the positive photoemission-induced surface charge from the grounded sample holder. However, surface charging in the 32 nm film was completely eliminated by annealing in activated oxygen at 500 °C to remove the surface contamination and the clean-surface binding energies for this film match those of the thicker films after the same oxygen annealing rather closely. Surface cleaning resulted in shifts of 0.25–0.35 eV to lower binding energy for all four films, indicating the onset of upward band bending of this magnitude (see Fig. S3).

Surface depletion of the magnitude expected based on Poisson analysis of the transport data [Fig. 1(b)] should also leave the near-surface region in an insulating state, resulting in surface charging in XPS. If this were the case, obtaining the spectra shown in Figs. 2 and S3 (for which the binding energies are accurately referenced to the Fermi level) would not have been possible. We have also measured ultraviolet photoelectron spectroscopy (UPS) using He I VUV light without any surface charging on h-MBE grown $La_{0.02}Sr_{0.98}TiO_3$(001) films.[15,19] UPS spectra are much more susceptible to charging than XPS because of the higher brightness of the VUV light source. Therefore, something other than conventional surface depletion is contributing to the electronic dead layers in these n-type STO homoepitaxial films. One possibility is polarization-induced dipole layers perpendicular to the surface. Such layers could trap itinerant charges, rendering the film insulating or at least highly resistive across the depth over which the polarization occurs. To test this hypothesis, we performed a near-surface structure determination using crystal truncation rod (CTR) measurements, along with coherent Bragg reflection analysis (COBRA), for a 15 u.c. homoepitaxial $Dy_{0.006}$ $Sr_{0.994}TiO_3$(001) film. This thickness was selected specifically for COBRA measurements to ensure good sensitivity to both the doped film and the undoped substrate below it.

Crystal truncation rod/COBRA analysis and first principles modeling

Excellent fits of the raw CTR data were achieved using COBRA, as shown in Fig. 3. The electron densities (ED) profiles generated from COBRA analysis show well-resolved, sharp peaks for Sr, Ti, and O atoms (see Fig. S4). The electron densities for all atoms are constant within the bulk STO and the film. However, we observe a slight dip in the Sr and Ti EDs at the substrate/film interface. It was previously reported that thickness fringes can appear in XRD for homoepitaxial STO films due to the presence of an interface offset.[20] This interface offset can cause laterally non-uniform lattice distortions. Since COBRA averages all lateral variations into a single "folded" unit cell based on the substrate crystal lattice,[21] a drop in ED is, thus, observed. This apparent drop at the substrate/film interface is also seen in the layer resolved integrated EDs, or electron numbers (EN), along the Sr and Ti columns (Fig. S5). Apart from this artifact, we observe essentially constant EN values for Sr, Ti, and

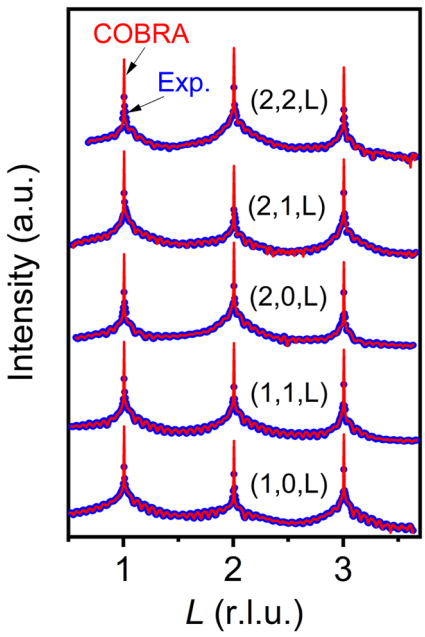

FIG. 3. Overlay of experimental CTRs (blue dots) and COBRA fits (solid red curves) for 15 u.c. $Dy_{0.006}$ $Sr_{0.994}TiO_3$/$SrTiO_3$(001).

both apical and equatorial O atoms; these match well with the corresponding atomic numbers (38, 22, and 8, respectively) throughout the homoepitaxial structure.

The atomic displacements extracted from COBRA analysis (Fig. 4) yield a polarization profile (Fig. 5) that clearly shows enhanced polar distortions near the film surface. Strong polar distortions near the surface could cause electron trapping, resulting in locally enhanced electron density near the surface region.[6,22] The change of sign in the polarization profile after the 13th u.c. indicates that some degree of polarization exists in the bulk of the film as well, which is likely to influence the electronic properties of the system, along with the surface polarization. The presence of an uncompensated electric field and changes in surface stoichiometry during cooling may be contributing factors to lattice polarization.[6]

We turn to first-principles modeling to determine the extent to which the lattice polarization could trap charge. Since O^{2-} anions are highly polarizable, the positions of their nuclei do not coincide with the positions of the maxima of their electron density, resulting in overestimated polarizations of the AO and BO_2 planes in COBRA. Since this error is smaller for cations, we used the positions of all Sr and Ti atoms as generated by COBRA. The positions of O anions were then linearly interpolated between their in-plane positions set according to the corresponding cation positions ($\mathbf{R}_0$) and their positions generated using COBRA ($\mathbf{R}_C$) as $\mathbf{R}(p) = p^*\mathbf{R}_C + (1 - p)^*\mathbf{R}_0$, where p is an interpolation parameter ($0 \le p \le 1$). Calculations of the average electrostatic potential profile across the slab [Fig. 6(a)] for $0.0 \le p \le 0.3$ show that as p (the magnitude of polarization associated with each atomic plane) increases, the potential in the central part of the film becomes lower than the potential near the surface and in the substrate, i.e., a polarization-induced potential well is formed. Calculations of the one-electron density of states (DOS) projected onto the orbitals of atoms in the TiO_2 planes [Fig. 6(b)] for the same interval of p show that the VB and CB band edges, while flat for $p = 0.0$ and $p = 0.1$, exhibit considerable bending at $p = 0.3$, further suggesting localization of the CB electrons. To visualize the effect of the polarization on the spatial distribution of the CB electrons, we calculated the charge density associated with states in the energy range between the CB minimum (E_C) and the Fermi level (E_F) and plotted the surfaces of constant density for each case in Fig. 6(c). We note that further increasing the value of p results in an additional shift of the DOS associated with the TiO_2 surface plane to higher energy leading to a closing of the bandgap.

As the magnitude of the simulated polarization (represented by the parameter p) increases, the preferred location of the CB electrons shifts from the surface (at $p = 0$) to a portion of the film closer to the buried interface (at $p = 0.3$). This localization is driven by lattice distortions as captured by COBRA. While this analysis does not reveal the atomic-scale origin of these distortions, it demonstrates that lattice distortions along [001] alone are sufficient to cause charge confinement along the surface normal in the n-STO film close to the buried interface.

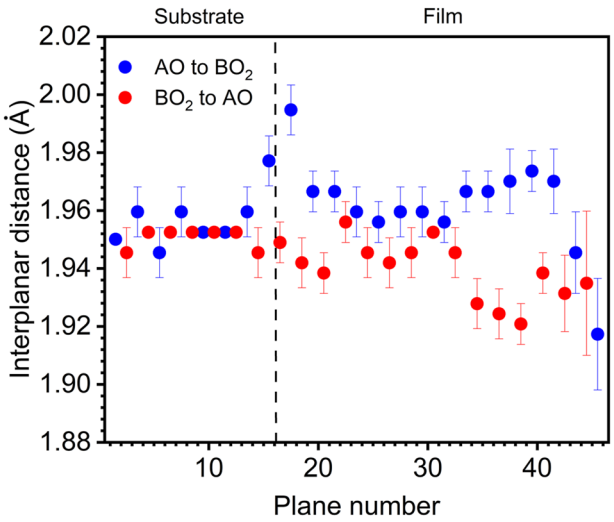

FIG. 4. Interplanar spacings between consecutive planes calculated using the z coordinates of the A-site cation (Sr) and B-site cation (Ti) for 15 u.c. $Dy_{0.006}Sr_{0.994}TiO_3/SrTiO_3(001)$ from COBRA. The dashed line shows the interface between the STO substrate and the film. These spacings within the substrate are constant and equal to 1.95 Å (3.905 Å × 0.5) within the analysis error range. However, we see an abrupt increase in the Sr-to-Ti interplanar spacings and a concomitant drop in Ti-to-Sr interplanar spacings at the substrate/film interface, indicative of the lattice distortions mentioned above. Moving away from the substrate/film interface, we continue to see fluctuations in Sr-to-Ti and Ti-to-Sr spacings that reveal lattice polarization. It is also evident that the distortions are more pronounced at the film surface than in the film interior.

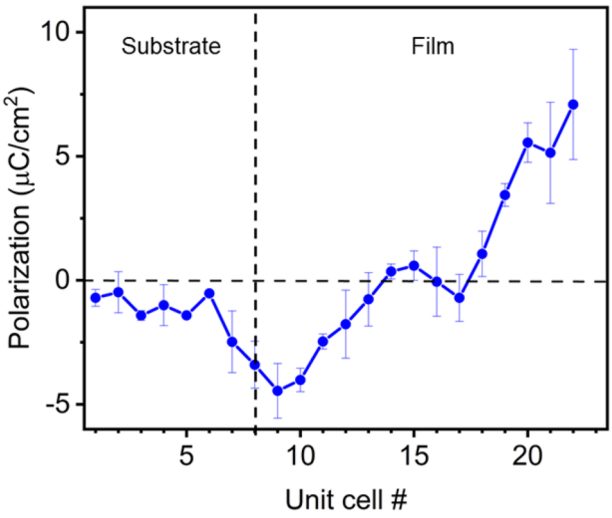

FIG. 5. Lattice polarization for 15 u.c. $Dy_{0.006}Sr_{0.994}TiO_3/SrTiO_3(001)$ as determined from vertical displacements of apical oxygens (O_a), equatorial oxygens (O_e), and B-site cations relative to the A-site cations in the same plane calculated from COBRA.

A classical electrostatic model of the buried interface

To probe the effect of lattice polarization from a different angle, we turn to an independent theoretical approach based on the solution of Maxwell's equations with appropriate boundary conditions. Fu *et al.*[23,24] have formulated a model that predicts the

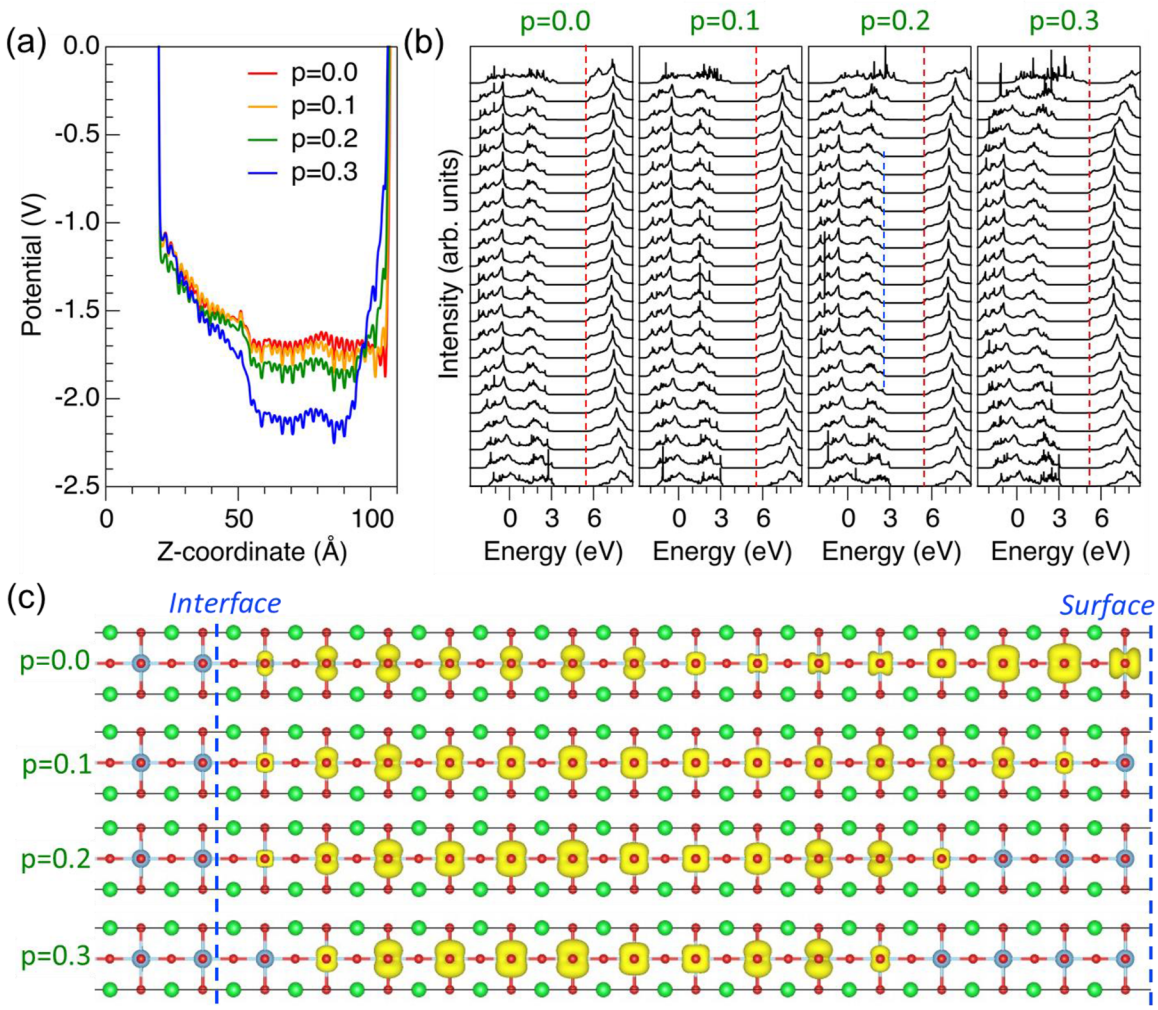

FIG. 6. Electronic structure and localization of the electron charge at CB minimum as a function of out-of-plane polarization for $Dy_{0.006}$ $Sr_{0.994}TiO_3/SrTiO_3(001)$. (a) Electrostatic potential profiles averaged over the in-plane direction (X–Y plane) and over approximately one unit cell along the off-plane direction (Z). (b) DOS projected on the TiO_2 planes; dashed lines mark the position of the CB minima for each p. (c) Surfaces of the constant charge density associated with the electronic states in the energy range: $E_C \le E \le E_F$. Sr, Ti, and O atoms are shown with green, blue, and red spheres, respectively. The interpolation parameter p is defined in the text.

sheet carrier density (n_{2D}) and electric potential (ϕ) as functions of distance from an n-STO/undoped STO(001) interface based on a Landau–Ginzburg free energy expansion of the lattice polarization and the Thomas–Fermi approximation for the electrons. This model assumes a strong nonlinear dielectric response to the built-in electric field that results from Fermi level equilibration at the interface and then calculates charge densities and potential profiles accordingly. Consider a homojunction in which both the n-STO and the undoped STO are several hundred nm thick and the carrier concentration in the n-STO is equal to the value measured for our set of $Dy_{0.001}Sr_{0.999}TiO_3$films on which we performed transport and XPS measurements (n_o = 2.1 × 10^{19} cm^{-3}). The model predicts charge transfer from n-STO to STO and the formation of an accumulation layer on the STO side. The carrier concentration, $n(z)$, exhibits an interfacial value of ~0.5n_o that decays with a characteristic length (d) in the accumulation region of 21 nm. As the thickness of the n-STO layer is reduced, the model predicts that the normalized carrier concentration within the n-STO film, $n(z)/n_o$, drops along with the effective sheet carrier concentration, as shown in Figs. 7(a) and 7(b). However, all three modeled films in Fig. 7(a) exhibit accumulation layers with long tails and we tentatively assign these as contributing to the electronic dead layers measured by transport.

However, the surface and/or lattice polarization can also play a role. Consider a film of thickness 40 nm for which the model predicts that n_{2D} = 5.5 × 10^{13} cm^{-2} [Fig. 7(b)]. For the same film, the critical value for n_{2D} at which the metal–insulator transition occurs at room temperature is given in this model by

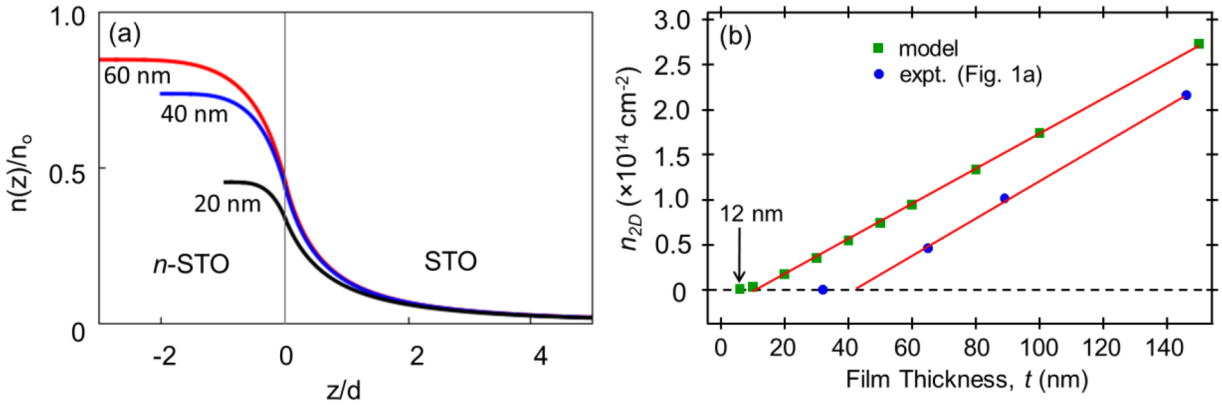

FIG. 7. Model predictions of the normalized carrier concentration (a) and sheet carrier density (b) for $Dy_{0.001}Sr_{0.999}TiO_3$/undoped STO(001) as a function of film thickness. Here, $n_o = 2 \times 10^{19}$ cm^{-3} and $d = 21$ nm. Comparison of the model prediction with transport data shows that for each film thickness, the actual sheet carrier density is ~5×10^{13} cm^{-2} less than that predicted by the model, revealing some charge immobilization either in the surface contamination layer or within the corrugated potential generated by lattice polarization. In the model, electrons that drift into the accumulation layer ($z/d > 0$) become part of the 12 nm dead layer.

$n_C = \beta \frac{N^{0.66}}{a_B} t = 1.2 \times 10^{13}$ cm^{-2}.[25] Here, N is the ionized donor concentration (2.1×10^{19} cm^{-3} in this case), a_B is the Bohr radius, t is the film thickness, and β = ~0.5. Based on these numbers, a 40 nm $Dy_{0.001}Sr_{0.999}TiO_3$ film should be metallic rather than insulating. The actual insulating character of such a film suggests that ~5×10^{13} cm^{-2} electrons are immobilized somewhere other than at the buried interface, either by acceptor states associated with surface contamination or by lattice polarization within the film. When t increases to 60 nm, the model predicts that $n_{2D} = 9.4 \times 10^{13}$ cm^{-2} and $n_C = 1.8 \times 10^{13}$ cm^{-2}. Therefore, even if ~5×10^{13} cm^{-2} electrons are immobilized at this surface, there are sufficient mobile carriers remaining for the film to be metallic. The same is true for thicker films. Thus, this model provides some insight into the observation of a 42 nm dead layer in the $Dy_{0.001}Sr_{0.999}TiO_3$ (001) film set.

To determine whether the built-in potential at the buried interface is sufficiently large to be detectable by hard x-ray photoelectron spectroscopy (HAXPES), we grew an 8 nm $La_{0.01}Sr_{0.99}TiO_3$ film on a 400 nm undoped STO film in turn grown on a $SrNb_{0.01}Ti_{0.99}O_3$(001) substrate. These thicknesses were chosen to provide sufficient n-STO and undoped STO layer depths for the electronic properties of the interface to be established while still being able to probe the interfacial region by HAXPES. The CL spectra are shown in the supplementary material (see Fig. S6) along with those measured for a flat-band $SrNb_{0.01}Ti_{0.99}O_3$(001) crystal. The Sr 3d and Ti 2p line shapes for the two samples are virtually identical, indicating no measurable band bending in the film within the probe depth. The full widths at half maximum for both CLs are quite low (e.g., 0.73 and 0.75 eV for Sr $3d_{5/2}$ for the bulk and the film samples, respectively) and they are the same, consistent with negligible band bending within the HAXPES probe depth. Based on previous XPS for heteroepitaxial STO/Ge(001) heterojunctions excited with AlKα x-rays,[18] we estimate the photoelectron attenuation lengths (λ) for Ti 2p and Sr 3d at $h\nu$ = 5.95 eV to be 6.3 and 6.6 nm, respectively. Defining the probe depth to be the distance over which 95% of the signal originates (numerically equal to 3λ), the Sr 3d and Ti 2p intensities carry information about built-in potentials to a depth of ~19–20 nm below the surface. Therefore, the measurements shown in Fig. S6 probe the entire 8 nm n-STO film and ~11–12 nm of the underlying undoped film. The absence of measurable band bending is understandable because our model calculations reveal that the potential drop across the 8 nm $La_{0.01}Sr_{0.99}TiO_3$ film and the first 11–12 nm of the undoped $SrTiO_3$(001) is only ~40 meV, as shown in Fig. S7. A 40 meV change in potential is not detectable with an instrumental resolution of 100 meV, the value for our HAXPES beamline and spectrometer.

In a related vein, this model also sheds light on why there is no detectable band bending at the film surfaces prior to cleaning (Fig. 2) if indeed ~5×10^{13} e$^-$/cm^{-2} are trapped in the surface contamination layer. Poisson's equation with κ = 300 predicts that this density of trapped charge would lead to depletion of the top 24 nm of the films and a total upward band bending of 0.36 eV. However, within the Sr $3d_{5/2}$ (Ti$2p_{3/2}$) probe depth of 5.7 nm (4.4 nm), the band bending would be 0.15 eV (0.12 eV), both of which are below the detection limit of XPS. Indeed, a simulation shows that the 0.15 eV band bending over a depth of 5.7 nm results in a binding energy shift of +0.04 eV relative to flat band and no measurable increase in peak width (see Fig. 8).

In addition, this model provides an explanation for why the 32 nm film was insulating as prepared in both photoemission and transport but became conductive upon surface cleaning (see Fig. S3), only to become insulating again following recontamination in lab air. If the insulating state results from charge trapping at the interface as well as at the unclean surface, then surface cleaning by heating in oxygen should at least partially restore the conductivity, which is clearly observed. Indeed, Fig. 7(b) shows that the model predicts a dead-layer thickness of 12 nm at the buried interface. As a result, the top 20 nm of the 32 nm film should be conductive once the surface-trapped charge is unbound by surface cleaning.

The principal shortcoming of this classical model is that, for each film thickness, electrons that drift into the accumulation layer

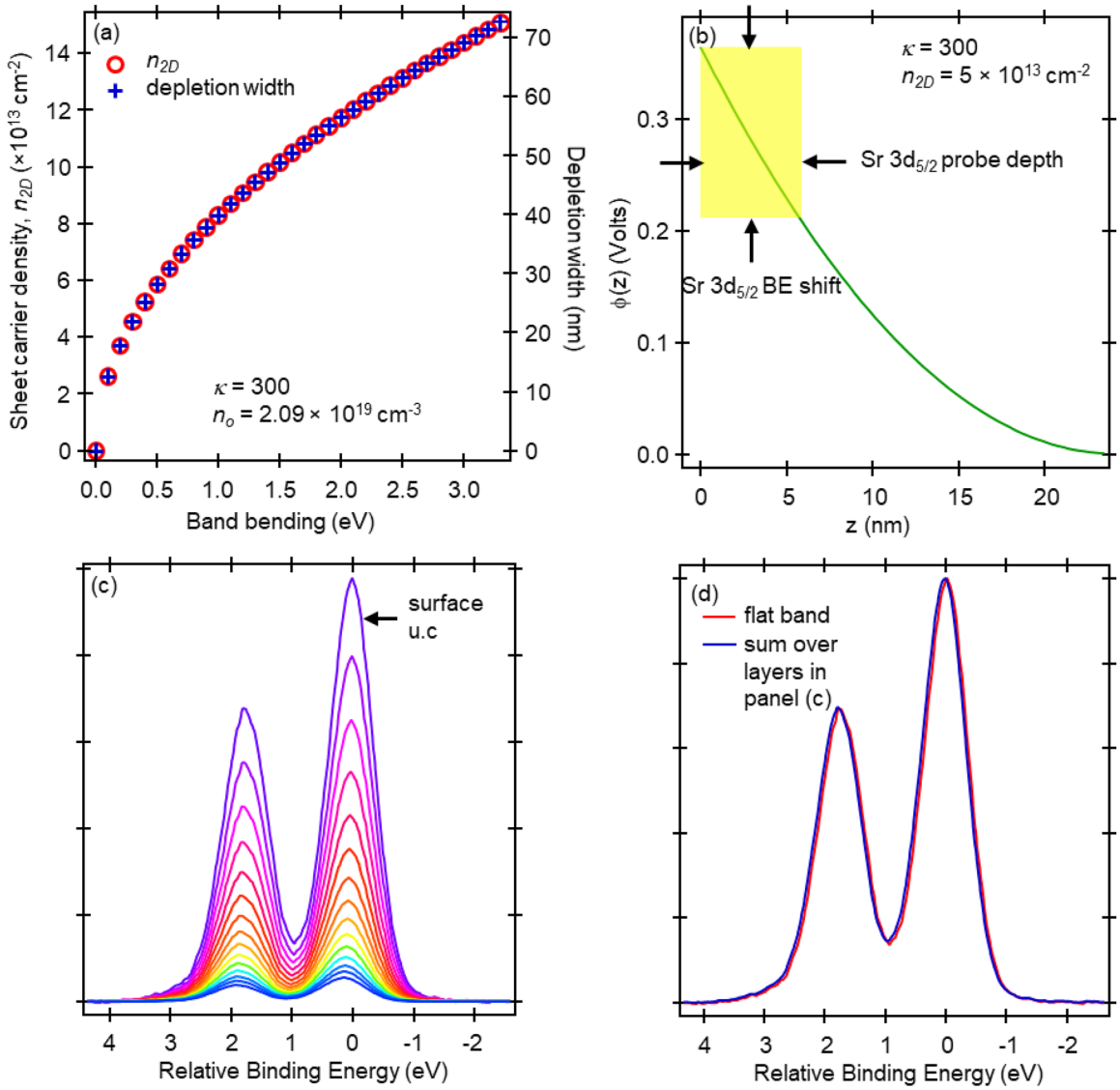

FIG. 8. Simulated Sr 3d line shape change based on the calculated depletion width and potential drop across the probe depth from the solution of Poisson's equation with a volume carrier concentration of 2.1 × 10^{19} cm^{-3} and a trapped electron density in the surface contamination layer of 5 × 10^{13} cm^{-2}. (a) Calculated sheet carrier density and depletion width vs band bending (the domain is a full span of possible band bending values based on the STO bandgap). (b) Surface potential vs depth specifically for n_{2D} = 5 × 10^{13} cm^{-2}. (c) Layer-resolved Sr 3d spectra with binding energies scaling with the potential drop across the probe depth shown in panel (b) [each spectrum is that measured for a flat-band $SrNb_{0.01}Ti_{0.99}O_3$ (001) bulk crystal attenuated according to the layer depth below the surface and shifted relative to the surface-layer spectrum according to the potential drop shown in panel (b)]. (d) Sum over layers from panel (c) along with the spectrum for the surface layer only (representing the flat-band condition). As shown in panel (d), the binding energy and the full width at half maximum increase by negligible amounts upon simulating the expected potential drop associated with trapped surface charge (blue) relative to those for the flat band condition (red).

[$z/d > 0$ in Fig. 7(a)] are naturally assigned as becoming part of the 12 nm dead layer shown in Fig. 7(b). However, there is no reason to think that electrons in the accumulation layer would be immobilized, except for those far enough from the interface that the carrier concentration is below the threshold for the metal–insulator transition observed by Spinelli *et al.*[26] Therefore, we suggest that electrons that drift to the interface become trapped by interface states, similar to what occurs at the *n*-GaAs/undoped GaAs(001) homojunction.[1] The nature and characteristics of these interface states are not known at present for the *n*-STO/STO system; characterizing and understanding these traps is a topic for future research.

CONCLUSIONS

In summary, we show that charge immobilization in homoepitaxial films of *n*-STO(001) occurs at both the buried *n*-STO/undoped STO interface and at the surface when the latter is contaminated due to air exposure. Analysis of results based on samples with air-exposed *and* clean surfaces is required to sort out the role of the surface in creating the dead layers. Carrier depletion exclusively at the surface can occur for *n*-STO films grown heteroepitaxially on other substrates for which charge transfer from the *n*-STO film to the underlying layer is prevented by the local electronic structure there (e.g., that caused by heterojunction formation).[7,27,28] However, in the homoepitaxial case, modeling based on classical electrostatics assuming a strong nonlinear dielectric response to the electric field that forms at the buried interface as Fermi level equilibration occurs suggests that both the surface and the buried interface are involved in the dead-layer formation and that neither results in sufficient band bending to be detectable by x-ray photoemission.

SUPPLEMENTARY MATERIAL

See the supplementary material for experimental and modeling information as well as supporting data.

ACKNOWLEDGMENTS

Work at PNNL was supported by the U.S. Department of Energy, Office of Science, Basic Energy Sciences (Award No. 10122). WSS acknowledges support from the OSU-PNNL Graduate Fellowship. Work at UMN was supported by the U.S. Department of Energy (Grant No. DE-SC002021). Structural characterizations were carried out at the University of Minnesota Characterization Facility, which receives partial support from NSF through the MRSEC program (Award No. DMR-2011401). ZY acknowledges support from the Air Force Office of Scientific Research (AFOSR) (Grant No. FA9550-21-1-0025). YH was supported by the Fine Theoretical Physics Institute of UMN. Modeling was done using the National Energy Research Scientific Computing Center, a DOE Office of Science User Facility supported by the Office of Science of the U.S. Department of Energy (Contract No. DE-AC02-05CH11231) using NERSC (Award No. BES-ERCAP0021800). This research used resources at the Advanced Photon Source, a U.S. Department of Energy (DOE) Office of Science user facility operated for the DOE Office of Science by Argonne National Laboratory (Contract No. DE-AC02-06CH11357).

AUTHOR DECLARATIONS

Conflict of Interest

The authors have no conflicts to disclose.

Author Contributions

S. A. Chambers: Conceptualization (lead); Data curation (equal); Formal analysis (equal); Funding acquisition (equal); Investigation (equal); Methodology (equal); Project administration (lead); Supervision (equal); Writing – original draft (lead); Writing – review & editing (lead). **D. Lee:** Data curation (equal); Formal analysis (equal); Investigation (equal). **Z. Yang:** Data curation (equal); Formal analysis (equal); Methodology (equal). **Y. Huang:** Data curation (equal); Formal analysis (equal); Investigation (equal). **W. Samarakoon:** Data curation (equal); Formal analysis (equal); Writing – original draft (equal). **H. Zhou:** Data curation (equal); Formal analysis (equal); Writing – original draft (equal). **P. V. Sushko:** Data curation (equal); Formal analysis (equal); Investigation (equal); Methodology (equal); Writing – original draft (equal); Writing – review & editing (equal). **T. K. Truttmann:** Data curation (equal); Formal analysis (equal). **L. W. Wangoh:** Data curation (equal); Formal analysis (equal). **T.-L. Lee:** Data curation (equal). **J. Gabel:** Data curation (equal). **B. Jalan:** Formal analysis (equal); Funding acquisition (equal); Supervision (equal); Writing – original draft (equal).

DATA AVAILABILITY

The data that support the findings of this study are available from the corresponding authors upon reasonable request.

REFERENCES

[1] D. C. Look, C. E. Stutz, and K. R. Evans, Appl. Phys. Lett. **56**, 668 (1990).
[2] W. E. Spicer, P. W. Chye, P. R. Skeath, C. Y. Su, and I. Lindau, J. Vac. Sci. Technol. **16**, 1422 (1979).
[3] H. H. Wieder, J. Vac. Sci. Technol. **17**, 1009 (1980).
[4] C. Kim, P. L. King, and P. Pianetta, J. Vac. Sci. Technol. B **10**, 1944 (1992).
[5] A. Ohtomo and H. Y. Hwang, Appl. Phys. Lett. **84**, 1716 (2004).
[6] Y. J. Shin, C. Lau, S. Lee, F. J. Walker, and C. H. Ahn, Appl. Phys. Lett. **115**, 161601 (2019).
[7] H. Jeong, N. G. Combs, S. Munyan, A. Rashidi, and S. Stemmer, Appl. Phys. Lett. **119**, 162601 (2021).
[8] S. A. Chambers, T. Ohsawa, C. M. Wang, I. Lyubinetsky, and J. E. Jaffe, Surf. Sci. **603**, 771 (2009).
[9] C. Capan, G. Y. Sun, M. E. Bowden, and S. A. Chambers, Appl. Phys. Lett. **100**, 052106 (2012).
[10] S. A. Chambers, M. Gu, P. V. Sushko, H. Yang, C. Wang, and N. D. Browning, Adv. Mater. **25**, 4001 (2013).
[11] S. A. Chambers and P. V. Sushko, Phys. Rev. Mater. **3**, 125803 (2019).
[12] Y. Aiura, I. Hase, H. Bando, T. Yasue, T. Saitoh, and D. S. Dessau, Surf. Sci. **515**, 61 (2002).
[13] R. A. Powell and W. E. Spicer, Phys. Rev. B **13**, 2601 (1976).
[14] B. Reihl, J. G. Bednorz, K. A. Müller, Y. Jugnet, G. Landgren, and J. F. Morar, Phys. Rev. B **30**, 803 (1984).
[15] S. A. Chambers, Y. Du, Z. Zhu, J. Wang, M. J. Wahila, L. F. J. Piper, A. Prakash, J. Yue, B. Jalan, S. R. Spurgeon, D. M. Kepaptsoglou, Q. M. Ramasse, and P. V. Sushko, Phys. Rev. B **97**, 245204 (2018).
[16] J. Son, P. Moetakef, B. Jalan, O. Bierwagen, N. J. Wright, R. Engel-Herbert, and S. Stemmer, Nat. Mater. **9**, 482 (2010).
[17] S. A. Chambers and P. V. Sushko, APL Mater. **7**, 110904 (2019).
[18] S. A. Chambers and Y. Du, J. Vac. Sci. Technol. A **38**, 043409 (2020).
[19] Z. Yang, D. Lee, J. Yue, J. Gabel, T.-L. Lee, R. D. James, S. Chambers, and B. Jalan, Proc. Nat. Acad. Sci. U. S. A. **119**, e2202189119 (2022).
[20] J. M. LeBeau, R. Engel-Herbert, B. Jalan, J. Cagnon, P. Moetakef, S. Stemmer, and G. B. Stephenson, Appl. Phys. Lett. **95**, 3243696 (2009).
[21] M. Sowwan, Y. Yacoby, J. Pitney, R. MacHarrie, M. Hong, J. Cross, D. A. Walko, R. Clarke, R. Pindak, and E. A. Stern, Phys. Rev. B **66**, 205311 (2002).

[22]K. Ahmadi-Majlan, T. J. Chen, Z. H. Lim, P. Conlin, R. Hensley, M. Chrysler, D. Su, H. H. Chen, D. P. Kumah, and J. H. Ngai, Appl. Phys. Lett. **112**, 5018069 (2018).
[23]K. V. Reich, M. Schecter, and B. I. Shklovskii, Phys. Rev. B **91**, 115303 (2015).
[24]H. Fu, K. V. Reich, and B. I. Shklovskii, J. Exp. Theor. Phys. **122**, 456 (2016).
[25]Y. Huang, Y. Ayino, and B. I. Shklovskii, Phys. Rev. Mater. **5**, 044606 (2021).
[26]A. Spinelli, M. A. Torija, C. Liu, C. Jan, and C. Leighton, Phys. Rev. B **81**, 155110 (2010).
[27]Z. H. Lim, N. F. Quackenbush, A. Penn, M. Chrysler, M. Bowden, Z. Zhu, J. M. Ablett, T.-L. Lee, J. M. LeBeau, J. C. Woicik, P. V. Sushko, S. A. Chambers, and J. H. Ngai, Phys. Rev. Lett. **123**, 026805 (2019).
[28]M. Chrysler, J. Gabel, T.-L. Lee, A. N. Penn, B. E. Matthews, D. M. Kepaptsoglou, Q. M. Ramasse, J. R. Paudel, R. K. Sah, J. D. Grassi, Z. Zhu, A. X. Gray, J. M. LeBeau, S. R. Spurgeon, S. A. Chambers, P. V. Sushko, and J. H. Ngai, Phys. Rev. Mater. **5**, 104603 (2021).